INTERNATIONAL JOURNAL FOR NUMERICAL METHODS IN FLUIDS, VOL. 18, 163–188 (1994)

MODELLING THE NON-LINEAR INTERACTION OF WIND AND TIDE: ITS INFLUENCE ON CURRENT PROFILES

A. M. DAVIES
Proudman Oceanographic Laboratory, Bidston Observatory, Birkenhead, Merseyside L43 7RA, U.K.

AND

J. LAWRENCE
MAFF, Fisheries Laboratory, Pakefield Road, Lowestoft, Suffolk NR33 OHT, U.K.

SUMMARY

A single-point model in the vertical is used to examine the coupling between tidal currents and wind-driven flows in shallow near-coastal regions. Calculations using both a linear slip and a no-slip condition at the sea bed clearly show that coupling between tidal and wind-driven currents cannot occur in a linear model with a time-independent eddy viscosity. However with a physically more realistic time-varying viscosity related to the flow field, coupling does occur, the magnitude of this non-linear interaction depending upon the change in eddy viscosity over a tidal cycle and the intensity of shear in the vertical. A point model in the vertical with flow induced by an oscillatory pressure gradient and an additional constant wind stress is used to examine the influence of viscosity parametrization and water depth upon this coupling.

The solution in the vertical is accomplished using both a functional approach and a finite difference method. Some conclusions as to the relative merits of these approaches, particularly the use of a transformed grid in the case of high-shear surface and bed boundary layers, are made in the paper.

KEY WORDS Non-linear interaction Hydrodynamic Spectral Finite difference Tidal current Wind-driven current

1. INTRODUCTION

Over the last 10–15 years an extensive number of three-dimensional simulations of tidal currents and detailed comparisons with observations have been carried out.[1–6] Although a number of three-dimensional wind-induced simulations have been performed[7–9] and three-dimensional flow fields have been examined, to the authors' knowledge no work has been done to examine the coupling of tidal and wind-driven currents in regions of significant tidal currents at a time of strong wind-driven flows. The lack of a detailed examination of this problem is surprising, since the coupling of tidal and wind-driven effects causes changes in sea surface elevation during major wind events (storm surges); the phenomenon of tide–surge interaction is well known and has been examined using a number of two-dimensional vertically integrated models.

In this paper a single-point model in the vertical driven by an oscillatory pressure gradient at tidal period together with surface wind stress forcing due to a constant wind stress is used to examine changes in tidal current profile at the fundamental period and the generation of

Received March 1993
Revised August 1993

higher tidal harmonics when a time-dependent eddy viscosity is used. Changes in wind-induced current profile due to this oscillatory tide are also examined.

Calculations are performed using both a time-invariant and a time-dependent eddy viscosity[10–12] with both a slip and a no-slip bottom boundary condition. A simple flow-related eddy viscosity is used here rather than one derived from a turbulence energy model[5] so that the processes coupling together tidal and wind-driven currents can be readily identified. The influence of eddy viscosity formulation, tidal forcing and water depth upon tidal and wind-driven coupling are examined.

Two different numerical methods are used in the vertical to compute the current profile, namely a functional approach[13–15] and a finite difference method. Some indication of the relative merits of each in problems involving two boundary layers, in this case the sea surface and sea bed, are made. Although a comparison of the functional and finite difference methods has been made previously in the case of tidal and wind wave problems (a single-boundary-layer problem),[16] to the authors' knowledge no such comparison has been made in the case of two boundary layers (sea surface and sea bed). The fact that the two approaches yield results that are not significantly different serves as a vital check that the non-linear mechanism proposed here does in fact have a major influence upon tidal and wind-induced current profiles, i.e. we are not seeing a spurious numerical result due to the numerical scheme but a real physical process.

2. HYDRODYNAMIC MODEL

2.1. *Hydrodynamic equations*

For a single-point model in the vertical driven by externally applied oscillatory pressure forcings of amplitudes H_x and H_y and phases g_x and g_y at period ω the hydrodynamic equations are given by[16]

$$\frac{\partial u}{\partial t} - \gamma v = \omega H_x \cos(\omega t + g_x) + \frac{\partial}{\partial z}\left(\mu \frac{\partial u}{\partial z}\right), \tag{1}$$

$$\frac{\partial v}{\partial t} + \gamma u = \omega H_y \cos(\omega t + g_y) + \frac{\partial}{\partial z}\left(\mu \frac{\partial v}{\partial z}\right). \tag{2}$$

In these equations u and v are the x- and y-components of current respectively, z is the vertical co-ordinate and t is time. The Coriolis parameter γ is constant and μ denotes the coefficient of eddy viscosity.

For wind-driven flow the surface stress is equal to the external wind stress components F_s and G_s, i.e.

$$-\rho\left(\mu \frac{\partial u}{\partial z}\right)_{\text{surface}} = F_s, \qquad -\rho\left(\mu \frac{\partial v}{\partial z}\right)_{\text{surface}} = G_s, \tag{3}$$

where ρ is the water density.

At the sea bed a no-slip condition can be applied, i.e.

$$u = v = 0, \tag{4}$$

or a bottom stress condition

$$-\rho\left(\mu \frac{\partial u}{\partial z}\right)_{\text{bed}} = F_B, \qquad -\rho\left(\mu \frac{\partial v}{\partial z}\right)_{\text{bed}} = G_B, \tag{5}$$

with F_B and G_B the bed stresses given by

$$F_B = k\rho U_h Q, \qquad G_B = k\rho V_h Q,$$

where k is the coefficient of bottom friction and U_h and V_h are the components of bottom current. For a linear slip bottom boundary condition

$$Q = 1, \tag{6}$$

while for quadratic slip

$$Q = (U_h^2 + V_h^2)^{1/2}. \tag{7}$$

2.2. Numerical solution using the Galerkin method

Since extensive details on solving the hydrodynamic equations using the Galerkin method in the vertical have been presented elsewhere,[14,15,17–19] we will only outline the major stages here, considering a mixed basis set. Thus the u and v-components of velocity are expanded as

$$U = \psi_u^s + \sum_{r=1}^{m} A_r(t) f_r(\sigma), \qquad V = \psi_v^s + \sum_{r=1}^{m} B_r(t) f_r(\sigma), \tag{8}$$

where ψ_u^s and ψ_v^s are additional functions specifically chosen to improve convergence in the near-surface layer, $f_r(\sigma)$ are chosen as eigenfunctions of the eddy viscosity profile,[15,17] $\sigma = z/h$ is the normalized vertical co-ordinate, with h the water depth, and $A_r(t)$ and $B_r(t)$ are coefficients to be determined using the Galerkin method. Having computed these coefficients, the current at any depth can be readily determined from expansion (8). The additional functions ('enhancement' functions) ψ_u^s and ψ_v^s were taken as the trigonometric functions used in Reference 15. Since extensive details of the formulation and application of the Galerkin method using such a 'mixed basis set' approach are given elsewhere,[15,17] they will not be repeated here.

2.3. Solution using a finite difference grid in the vertical

In the case of a no-slip condition at the sea bed it is advantageous to use a transformation which transforms equations (1) and (2) in such a manner that discretizing the transformed equations on a regularly spaced finite difference grid in the vertical is physically equivalent to using a grid with enhanced resolution in the near-bed region.

Appropriate transformations on to a co-ordinate s are either logarithmic of the form

$$s = \ln (z/S_0)/\beta, \quad \text{with } \beta = \ln (h/S_0), \tag{9}$$

or log–linear of the form

$$s = \left[\ln\left(\frac{z}{S_0}\right) + \left(\frac{z - S_0}{S_*}\right)\right]\Big/\beta, \quad \text{with } \beta = \ln\left(\frac{h}{S_0}\right) + \frac{h - S_0}{S_*}. \tag{10}$$

In these transformations h is the water depth and S_0 is a small parameter which removes the logarithmic singularity at $z = 0$ and determines the degree of grid resolution in the near-bed region. The parameter S_* in the log–linear transformation is an arbitrary height above the sea bed over which the grid is essentially logarithmic.

It can be readily shown from (9) that

$$\frac{\partial}{\partial z} = \frac{1}{\chi}\frac{\partial}{\partial s}, \quad \text{with } \chi = S_0 \beta e^{\beta s}. \tag{11}$$

Using equation (1) for illustrative purposes, transforming gives

$$\frac{\partial u}{\partial t} - \gamma v = \omega H_x \cos(\omega t + g_x) + \frac{1}{\chi}\frac{\partial}{\partial s}\left(\frac{\mu}{\chi}\frac{\partial u}{\partial s}\right). \tag{12}$$

The numerical solution of equation (12) can be readily accomplished using the Crank–Nicolson method in the time domain with a finite difference grid in the vertical.

Thus at the kth grid point we have

$$\frac{U_k^{t+\tau} - U_k^t}{\tau} - \gamma V_k^{t+0{\cdot}5\tau} = \omega H_x \cos[\omega(t + \theta_1 \tau) + g_x] + \frac{\theta_1 W_k}{\Delta^2}(\mu_k^t \bar{W}_k \delta U_k^{t+\tau} - \mu_{k-1}^t \bar{W}_{k-1} \delta U_{k-1}^{t+\tau})$$

$$+ \frac{\theta_2 W_k}{\Delta^2}(\mu_k^t \bar{W}_k \delta U_k^t - \mu_{k-1}^t \bar{W}_{k-1} \delta U_{k-1}^t), \tag{13}$$

where $\delta U_k = U_{k+1} - U_k$ and Δ is the vertical grid spacing. A staggered finite difference grid with respect to viscosity and flow has been used in the vertical (see Figure 1). Also, $W_k = 1/\chi$ evaluated at u-grid point k and $\bar{W}_k = 1/\chi$ evaluated at the midpoint between u-grid points $k + 1$ and k (see Figure 1).

In equation (13) θ_1 lies in the range $0 \leqslant \theta_1 \leqslant 1$ and $\theta_2 = 0{\cdot}1 - \theta_1$, giving a time-centred solution when $\theta_1 = \theta_2 = 0{\cdot}5$ (the Crank–Nicolson method) and an implicit solution when $\theta_1 = 1{\cdot}0$ and $\theta_2 = 0{\cdot}0$.

Davies[16] demonstrated the advantages of using the logarithmic or log–linear transformation to give a high grid resolution in the bottom boundary layer when a no-slip condition was used at the sea bed with tidal or wind wave forcing. The application of a functional approach with a no-slip condition is given in Reference 20.

In this paper we consider the use of a similar transformation in the surface boundary layer with S_1 a parameter which determines the degree of grid resolution in the near-surface layer when wind forcing is applied. Also, an irregular grid spacing can be used with a logarithmic-type grid in the surface and bed boundary layers with spacing determined by S_1 (near-surface grid) and S_0 (near-bed grid) when both wind and tidal forcing are applied with slip or no-slip conditions.

3. NUMERICAL CALCULATIONS

3.1. *Eddy viscosity formulation for wind- and tidally-forced flows*

There are two primary objectives of the series of calculations presented in this section. The first is to examine the accuracy of using finite difference grids, either uniform or irregular (in

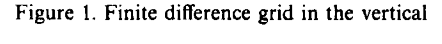

Figure 1. Finite difference grid in the vertical

the sense of having enhanced resolution in the near-surface and near-bed regions), to simulate a combination of tidal and wind-driven flows and to compare results from these with a functional approach. The second, having ensured that an accurate solution can be obtained (the first objective), is to examine how tidal and wind-driven current profiles are modified by a flow-dependent eddy viscosity depending upon the total current.

In an initial series of calculations we assume that the eddy viscosity does not vary in the vertical (Figure 2, profile A). Although such a profile is acceptable away from the surface and bed boundary layers, a more general profile (Figure 2, profile B) is one in which the eddy viscosity decreases in the near-bed region to a value μ_0 reflecting a wall boundary layer. Just what form the eddy viscosity should take in the near-surface layer during major wind forcing is difficult to determine. If the surface is assumed to be a wall layer, then the eddy viscosity should decrease. However, during a large wind event the surface can be regarded as a source of turbulence as the wind wave breaks and the viscosity should increase in this layer.[21] In view of this uncertainty, the viscosity in the surface layer was maintained at the same value as in the bulk of the water column.

Measurements[11,12] suggest that in the near-bed region the turbulence decreases over a distance h_1 of order 0·2h.

At the sea bed μ_0 is given by

$$\mu_0 = K_0 U_* Z_0, \tag{14}$$

where $K_0 = 0{\cdot}4$ is Von Karman's constant, U_* is the frictional velocity of order 2–4 cm s^{-1} and Z_0 is the roughness length of order 0·01–0·001 m, giving μ_0 of order 0·0001 m^2 s^{-1}.

Away from the boundary layers the eddy viscosity μ_1 is given by

$$\mu_1 = 0{\cdot}0025h|\bar{u}|, \tag{15}$$

where $\bar{u}$ is the depth-mean current.

In shallow seas, i.e. water depths typically of order $h = 40$ m, tidal and wind-driven current velocities are of order $u = 1$ m s^{-1}. Substituting these values in (15), we obtain $\mu_1 = 0{\cdot}1$ m^2 s^{-1}.

An alternative viscosity formulation (appropriate in deep water where the length scale is not limited by the water depth h but is determined by the boundary layer thickness Δ) is to express μ_1 as[22]

$$\mu_1 = 0{\cdot}0025\Delta|\bar{u}|, \tag{16}$$

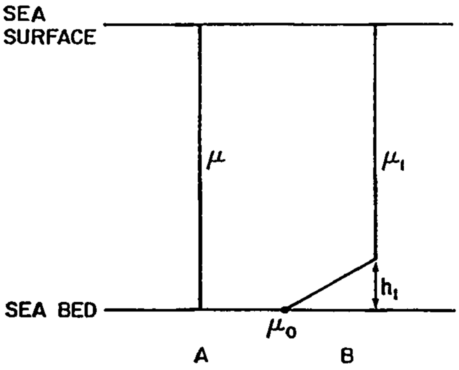

Figure 2. Profiles of eddy viscosity used in the calculations

where

$$\Delta = C(U_*/\omega_1),$$

with $\omega_1 = 10^{-4}\ \mathrm{s}^{-1}$ a typical frequency and $C = 0{\cdot}3$ a constant. Taking U_* as $2\ \mathrm{cm\ s^{-1}}$ gives $\mu_1 = 0{\cdot}15\ \mathrm{m^2\ s^{-1}}$. In the series of calculations described later using profile B, we take $\mu_1 = 0{\cdot}1\ \mathrm{m^2\ s^{-1}}$ and $\mu_0 = 0{\cdot}0001\ \mathrm{m^2\ s^{-1}}$.

An alternative formulation to equations (15) and (16), although it can be shown in deep water to be equivalent to (16),[22] is to express μ_1 as

$$\mu_1 = K_2\bar{u}^2/\omega_1, \tag{17}$$

with $K_2 = 2{\cdot}0 \times 10^{-5}$ a dimensionless coefficient. Both equations (15) and (17) are used later in time-varying eddy viscosity calculations.

3.2. Calculations using a time-invariant eddy viscosity

In an initial series of calculations a time-invariant eddy viscosity in the vertical (profile A, Figure 2) was used with a linear slip condition at the sea bed (equation (6)) and $k = 0{\cdot}002\ \mathrm{m\ s^{-1}}$. Two water depths, namely a shallow near-coastal depth $h = 10$ m and a deeper offshore depth $h = 100$ m, were used in the calculation, with a range of eddy viscosity values, namely $\mu = 0{\cdot}1$, $0{\cdot}01$ and $0{\cdot}005\ \mathrm{m^2\ s^{-1}}$. Calculations were performed using a uniform grid spacing, with the number N of finite difference grids taking a range of values, namely $N = 20, 40, 60, 80$ and 100, giving $\Delta\sigma$ ranging from 0·05 to 0·01. Calculations were also performed using an irregular grid spacing which was log–linear in the near-surface and near-bed boundary layers, giving the minimum $\Delta\sigma$ shown in Table I in the near-surface and near-bed boundary layers.

As a check on the accuracy of the finite difference solution, the calculations were also performed using the functional expansion initially without an 'enhancement' function, although subsequently such a function was used. Davies[15,16] showed that an accurate wind-driven surface current even with a low surface eddy viscosity value (μ of order $0{\cdot}01\ \mathrm{m^2\ s^{-1}}$) could be obtained using six eigenfunctions in the vertical and one 'enhancement' function. Such an expansion was used here, with the accuracy of both the finite difference and the Galerkin method checked using an expansion of 30 eigenfunctions with an additional 'enhancement' function.

Motion was started from a state of rest by the simultaneous application of a unit pressure forcing of 12 h period (diurnal period denoted by D_2) in the x-direction, i.e. $H_x = 1{\cdot}0\ \mathrm{m\ s^{-1}}$, $H_y = 0{\cdot}0$, $g_x = 0{\cdot}0$ and $g_y = 0{\cdot}0$ in equations (1) and (2), and a unit wind stress in the same direction, i.e. $F_s = 1{\cdot}0\ \mathrm{N\ m^{-2}}$ and $G_s = 0{\cdot}0$. In these calculations the effects of rotation were removed, i.e. $\gamma = 0{\cdot}0$ in equations (1) and (2). A time step of 6 min was used in all the calculations, although Davies[16] has shown that the Crank–Nicolson method is stable with a time step of order 30 min, but the solution is inaccurate with such a large time step.

Since motion was started from rest by the sudden application of both pressure and wind forcing, it was necessary to integrate forward in time for the order of a few tidal periods (six periods in shallow water and 12 periods in deep water) before the influence of the initial conditions was removed and a periodic solution superimposed upon a steady flow was obtained (although in the case of deep water, $h = 100$ m, with low viscosity the solution had only reached a 'near-steady state'). Once such a state was reached, a Fourier analysis was then performed using computed currents at each time step over a 12 h period in order to determine the magnitude of the residual current (denoted by D_0), the amplitude and phase of the fundamental and, in the case of time-varying viscosity (see later), the higher harmonics.

Table I. Magnitudes of surface ($\sigma = 1{\cdot}0$) and bed ($\sigma = 0{\cdot}0$) residual (D_0) and tidal (D_2) components of current in water depths (a) $h = 10$ m and (b) $h = 100$ m computed using finite difference and functional approaches

(a)	$h = 10$ m									(b)	$h = 100$ m								
	$\mu = 0{\cdot}01$ m^2 s^{-1}				$\mu = 0{\cdot}005$ m^2 s^{-1}						$\mu = 0{\cdot}01$ m^2 s^{-1}				$\mu = 0{\cdot}005$ m^2 s^{-1}				
	D_0(cm s^{-1})		D_2(cm s^{-1})		D_0(cm s^{-1})		D_2(cm s^{-1})		Minimum		D_0(cm s^{-1})		D_2(cm s^{-1})		D_0(cm s^{-1})		D_2(cm s^{-1})		Minimum
N or m	$\sigma = 1{\cdot}0$	$\sigma = 0{\cdot}0$	$\sigma = 1{\cdot}0$	$\sigma = 0{\cdot}0$	$\sigma = 1{\cdot}0$	$\sigma = 0{\cdot}0$	$\sigma = 1{\cdot}0$	$\sigma = 0{\cdot}0$	$\Delta\sigma_m$	N or m	$\sigma = 1{\cdot}0$	$\sigma = 0{\cdot}0$	$\sigma = 1{\cdot}0$	$\sigma = 0{\cdot}0$	$\sigma = 1{\cdot}0$	$\sigma = 0{\cdot}0$	$\sigma 1{\cdot}0$	$\sigma = 0{\cdot}0$	$\Delta\sigma_m$
20	144	46	87	43	239	44	101	32	0·05	20	921	22	103	21	1489	1	108	2	0·05
40	145	48	88	44	242	46	102	34	0·025	40	921	32	103	31	1474	15	109	16	0·025
60	146	48	89	44	242	47	102	35	0·1667	60	921	34	103	34	1468	19	109	22	0·0167
80	146	48	89	44	243	48	103	35	0·0125	80	921	36	103	34	1465	21	109	24	0·0125
100	146	48	89	44	243	48	103	35	0·01	100	921	37	103	37	1463	23	109	26	0·01
Irregular grid																			
20	146	49	89	45	244	49	103	36	0·0195	20	921	36	103	33	1469	18	109	20	0·0195
40	146	49	89	45	245	49	103	36	0·0036	40	921	40	103	39	1459	26	109	30	0·0036
60	147	49	90	45	245	49	103	36	0·0014	60	921	41	103	40	1458	27	109	31	0·0014
100	147	49	90	45	245	49	103	36	0·0006	100	923	41	103	41	1457	27	109	32	0·0006
										150	923	41	103	41	1459	28	109	32	0·0002
Galerkin method without 'enhancement' function																			
10	142	49	88	45	236	49	100	36		10	886	41	104	47	1395	28	110	40	
20	144	49	88	44	240	49	101	35		20	901	41	103	43	1417	28	109	35	
Galerkin method with 'enhancement' function																			
6	144	49	88	45	239	49	101	35		6	901	41	105	54	1433	28	114	52	
30	147	49	88	45	244	49	101	35		30	912	41	103	42	1438	28	109	32	

In the present case the eddy viscosity is time-invariant and consequently only the amplitude of the residual (D_0) fundamental period (period D_2) was non-zero. However, in the case of a flow-dependent eddy viscosity, other higher harmonics (denoted by D_4 with a period of 6 h and D_6 with a period of 3 h) could be generated.

In an initial series of calculations the eddy viscosity was fixed at $0{\cdot}1\ \mathrm{m^2\,s^{-1}}$ with $k = 0{\cdot}002\ \mathrm{m\,s^{-1}}$. Computed tidal and wind-induced currents determined using a uniform grid with $N = 20$ or 100 were not significantly different and were in good agreement with those determined using a variable double-long–linear transformation in the vertical with enhanced resolution in the boundary layers and the functional approach.

As expected from the surface and bed boundary conditions (equations (3) and (5)), if we apply a simple stress balance $\mu\partial u/\partial z = F$, with F an applied external surface stress, then when μ is high, $\partial u/\partial z$ will be low and there will no high-shear surface or bed boundary layer requiring a fine grid to accurately resolve it.

As stated previously, in any problem involving a time-dependent eddy viscosity related to the flow field (equations (15) and (17)), when the currents are low, the eddy viscosity will be small and the shear in the surface and bed boundary layers can be very large, requiring the use of a fine grid. To test the accuracy of the finite difference method and the functional approach with low viscosity, the previous calculations were repeated with $\mu = 0{\cdot}01$ and $0{\cdot}0050\ \mathrm{m^2\,s^{-1}}$. Profiles of the wind-induced current in both water depths (Figure 3) show that the shear in the surface and bed layers increases as expected as the eddy viscosity decreases. In the case of the amplitude of the D_2-component of the tide, it is shear-free in the surface layer but the shear in the near-bed layer increases as the eddy viscosity is reduced.

The magnitude of the wind-induced current (D_0) and the amplitude of the D_2-component of the tide at the surface and bed computed using the uniform grid, the double-log–linear transformation and the functional approach are given in Table I. Considering initially Table I(a), water depth $h = 10$ m, it is evident that for a given eddy viscosity magnitude, as the number of grid boxes increases in the uniform distribution, the surface and bed wind-induced currents converge towards those computed with the functional approach as the surface and bed shear layers are more accurately resolved. In the case of tidal currents, where the profile is shear-free in the surface layer (Figure 3), enhancing the resolution has little effect upon the tidal surface current. In the case of bed currents the frictional retarding force of the sea bed produces a sheared layer in both the wind-induced and tidally induced currents (Figure 3) which must be resolved in the model. As expected, using an irregular finite difference grid with enhanced resolution in the surface and bed layers improves the resolution in these layers, particularly with lower ($\mu = 0{\cdot}005\ \mathrm{m^2\,s^{-1}}$) eddy viscosity. As the eddy viscosity is reduced, the surface and bed layers become more highly sheared and hence the resolution in these layers must increase. Calculations using the Galerkin approach without an enhancement function show a slow convergence of the wind-driven current with $\mu = 0{\cdot}005\ \mathrm{m^2\,s^{-1}}$, although with the enhancement function a rapid rate of convergence is obtained, with six functions giving the same as 20 functions using eigenfunctions only, and in excellent agreement with that obtained using the irregular grid finite difference method.

In these calculations the enhancement function was chosen to increase the rate of convergence in the surface layer. However, increased convergence in the bed layer could be obtained by using functions which depend upon the bed stress.[17]

In deeper water, $h = 100$ m, particularly with low viscosity $\mu = 0{\cdot}005\ \mathrm{m^2\,s^{-1}}$, a true periodic condition had not been achieved after 2640 time steps (132 h). However, this 'near-steady state' was analysed in all cases in order to determine the rate of convergence of the various approaches. It is evident (Table I(b)) that with $\mu = 0{\cdot}005\ \mathrm{m^2\,s^{-1}}$ both tidal and wind-driven bed currents

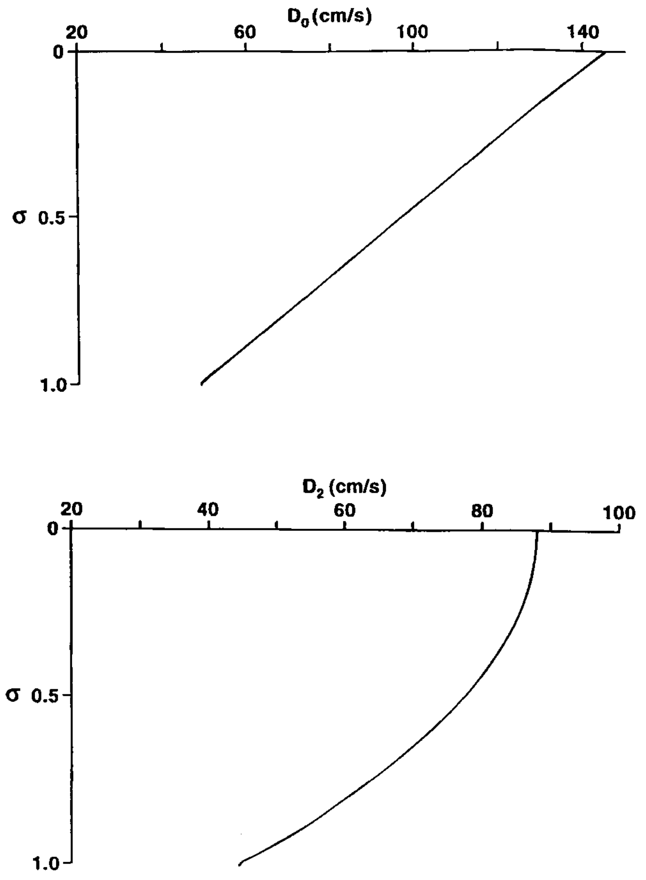

Figure 3(a). Profiles of residual wind-driven current (D_0) and amplitude of D_2-component of tide computed with $\mu = 0{\cdot}01\ \mathrm{m}^2\,\mathrm{s}^{-1}$, $h = 10$ m.

converge slowly and that as the grid is refined, the bed current increases, thus raising the bed stress and reducing the surface current. Calculations using the irregular grid show that with such a distribution the solution computed using $N = 20$ is comparable with that for $N = 60$ on a regular grid. Calculations using an irregular grid with various S_0-values giving enhanced surface and bed resolution (i.e. a smaller $\Delta\sigma_m$) show solutions consistent with those obtained using an irregular grid with $N = 100$ (Table I(b)).

Wind-driven surface currents computed using the Galerkin approach without the enhancement function show a very slow rate of convergence, with current values below those computed with the finite difference approach. However, including the enhancement function gives a much faster rate of convergence, although surface currents are still slightly below those computed with the finite difference method (Table I(b)).

Although these calculations have involved the use of a flow-independent and hence time-invariant eddy viscosity with linear bottom friction, they do show that in the case of a flow-dependent viscosity it is essential to have high resolution in the boundary layers to account for the high-shear layers that can occur at times of low current and hence low viscosity. Since the

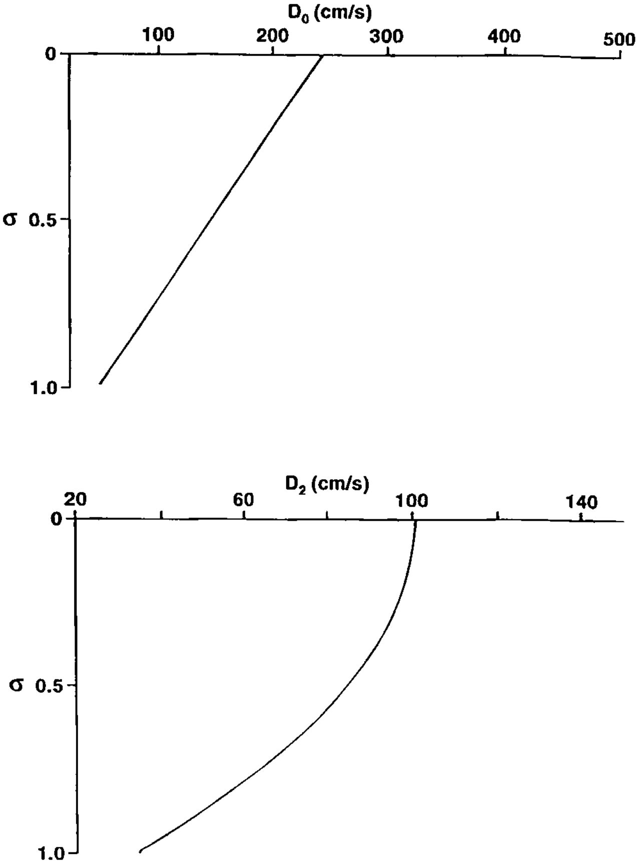

Figure 3(b). As Figure 3(a) but with $\mu = 0{\cdot}0050\ \mathrm{m}^2\,\mathrm{s}^{-1}$, $h = 10$ m.

eddy viscosity is independent of the flow field and the bottom friction is linear, no coupling occurs in the linear model used here between the wind-induced and tidal currents and hence no higher harmonics are produced. The solutions computed here are identical to those obtained by running the model with tidal or wind forcing alone.

In the case of a time-dependent eddy viscosity produced by tidal flows, Davies[16] showed that an accurate solution could be obtained by using a fine grid in the near-bed region. In the present series of calculations where we are considering tidal and wind-induced flows in combination, the presence of surface and bed shear layers requires a double-logarithmic layer with the order of 50–100 grid boxes in the vertical to accurately resolve the shear in these layers at times of low viscosity. In the next series of calculations with time-dependent viscosities a grid of this resolution (namely $N = 100$) was used in the vertical.

3.3. Calculations using a flow-dependent time-varying eddy viscosity

Unidirectional flow with a slip condition (viscosity profile A). In this series of calculations we again consider only unidirectional flow (the x-direction) by setting $\gamma = 0{\cdot}0$, and tidal forcing at

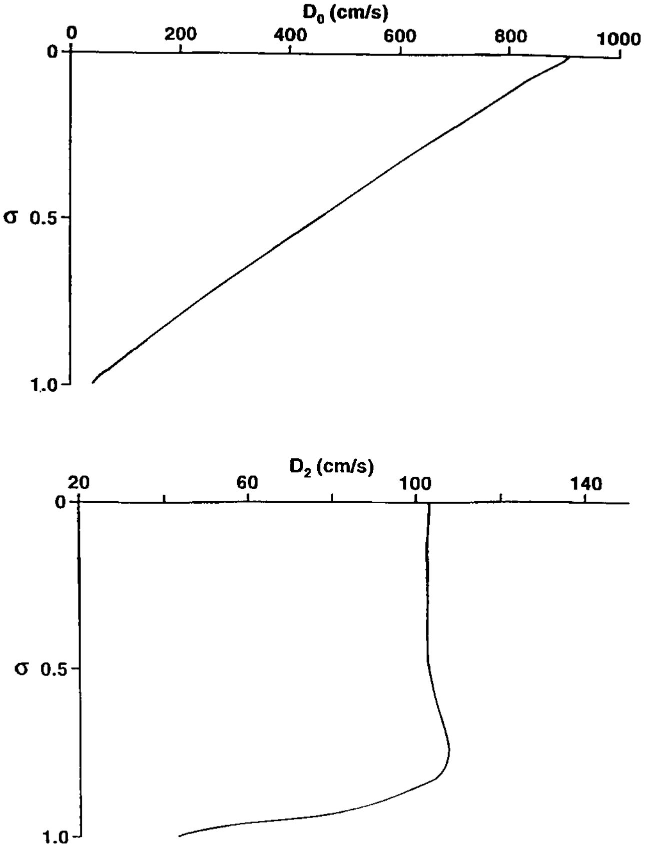

Figure 3(c). As Figure 3(a) but with $\mu = 0{\cdot}01\ \mathrm{m^2\,s^{-1}}$, $h = 100$ m.

the D_2-period of $H_x = 1{\cdot}0\ \mathrm{m\,s^{-1}}$, $H_y = 0{\cdot}0$, $g_x = 0{\cdot}0$ and $g_y = 0{\cdot}0$ with a superimposed unidirectional wind stress $F_s = 1{\cdot}0\ \mathrm{N\,m^{-2}}$ and $G_s = 0{\cdot}0$. However, in these calculations the eddy viscosity is not constant but evolves with the flow field according to equation (15), i.e. an $h|\bar{u}|$-dependent viscosity. Since the eddy viscosity varies with the flow field and consequently with time, the wind-induced and tidally induced currents are no longer independent; also, the non-linearity introduced by the time-varying viscosity (the only non-linearity if the equations are solved subject to a no-slip or a linear slip condition) generates higher tidal harmonics, principally at the periods D_4 and D_6.

Consider initially eddy viscosity profile A with a linear slip condition ($k = 0{\cdot}002\ \mathrm{m\,s^{-1}}$) and an $h|\bar{u}|$-dependent viscosity (equation (15)) in water depths of 10 and 100 m (Table II). The wind-induced currents (D_0) and the amplitude and phase of the harmonics D_2, D_4 and D_6 at surface, near-surface, mid-depth and bed in a water depth $h = 10$ m with $\mu \propto h|\bar{u}|$ computed with a uniform grid or a double-log-linear grid with $N = 100$ are not significantly different and are in excellent agreement with those determined using the functional approach (Table II).

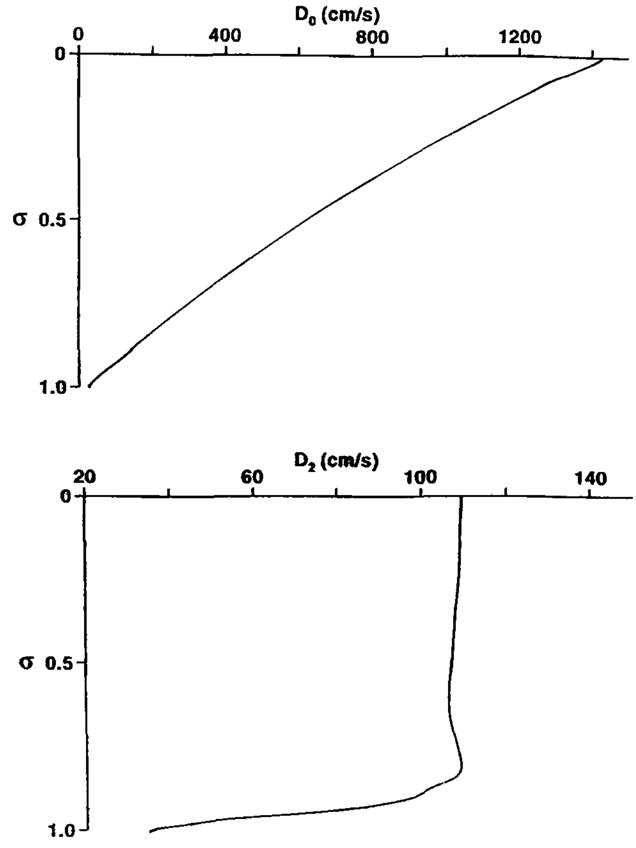

Figure 3(d). As Figure 3(a) but with $\mu = 0{\cdot}0050\ \mathrm{m^2\,s^{-1}}$, $h = 100$ m using a slip condition

It is interesting to note that as in the previous calculation in which the eddy viscosity was constant, the wind-induced current profile shows a decrease in magnitude from sea surface to sea bed (Table II, Figure 4(a)). The amplitude of the D_2-tide, however, no longer increases with height above the sea bed, with a shear-free region close to the sea surface, but shows a mid-water maximum with a decrease towards the sea surface (Table II, Figure 4(a)). Also, the D_4- and D_6-components of current are generated by the non-linearity produced by a time-varying eddy viscosity. These components are at a maximum near the sea surface where the shear is largest and hence the non-linear term $\mu \partial u/\partial z$ is a maximum.

In deeper water, $h = 100$ m, with $\mu \propto h|\bar{u}|$ some differences in wind-induced and tidally forced surface currents computed with $N = 100$ using a uniform grid and a double-log–linear grid are evident (Table II), although currents computed with the double-log–linear grid are in excellent agreement with those obtained using the functional approach (Table II). In all cases the current profiles show the same characteristics as those found in shallow water, namely a uniform decrease in wind-driven currents below the surface layer, with the D_2-tidal current having a maximum

Table II. Amplitude H (cm s^{-1}) and phase g (deg) of residual D_0, fundamental D_2 and higher harmonics D_4 and D_6 computed using finite difference and functional approaches at various water depths σ. Calculations were performed using a slip condition at the sea bed with h = 10 and 100 m

		Uniform finite difference				Transformed finite difference				Functional method			
σ		D_0	D_2	D_4	D_6	D_0	D_2	D_4	D_6	D_0	D_2	D_4	D_6
$(a)\ \mu \propto h\lvert\bar{u}\rvert,\ h = 10\ m$													
1·0	H	109	38	10	5	110	40	10	5	108	39	10	5
	g	—	210	87	132	—	211	89	136	—	210	90	136
0·99	H	108	39	9	5	109	41	9	4	108	39	9	5
	g	—	211	88	132	—	212	89	136	—	210	89	136
0·50	H	73	64	3	2	74	65	3	2	72	65	3	2
	g	—	215	261	210	—	216	261	310	—	215	262	313
0·0	H	49	58	0	0	50	60	0	0	49	59	1	1
	g	—	216	—	—	—	217	—	—	—	216	336	38
$(b)\ \mu \propto h\lvert\bar{u}\rvert,\ h = 100\ m$													
1·0	H	112	67	16	25	104	79	0	8	102	82	0	7
	g	—	266	81	111	—	257	—	98	—	257	—	102
0·99	H	103	80	0	8	102	82	0	7	101	83	0	7
	g	—	258	—	103	—	257	—	102	—	257	—	102
0·50	H	65	105	2	0	65	105	0	1	65	105	0	1
	g	—	263	62	—	—	263	—	271	—	263	—	274
0·0	H	49	86	5	0	49	87	0	0	49	87	0	0
	g	—	261	183	—	—	261	—	—	—	261	—	—

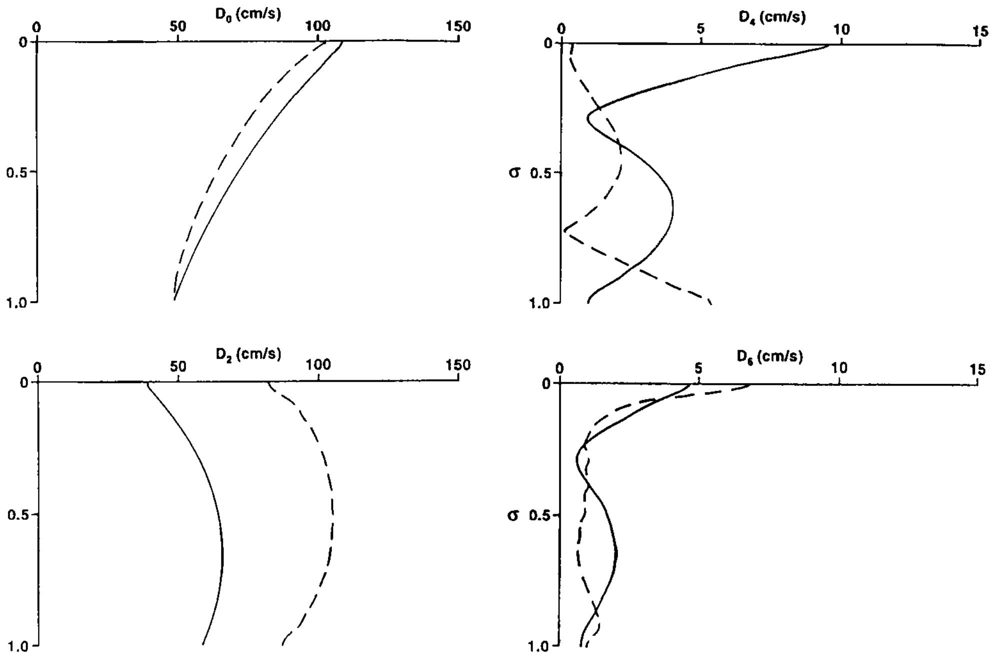

Figure 4(a). Profiles of residual current (D_0) and harmonics D_2, D_4 and D_6 computed with an $h|\bar{u}|$-dependent viscosity in water depths h = 10 m (——) and h = 100 m (– – –) using a slip condition

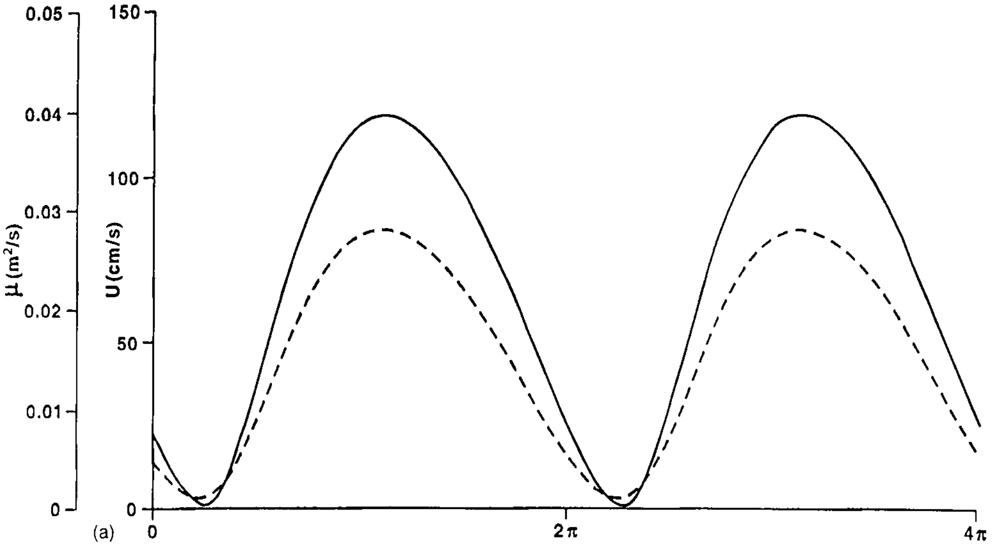

Figure 4(b). Time series of mid-depth current (——) and eddy viscosity (- - -) over two tidal cycles computed using $\mu \propto h|\bar{u}|$ with $h = 10$ m and a slip bottom boundary condition

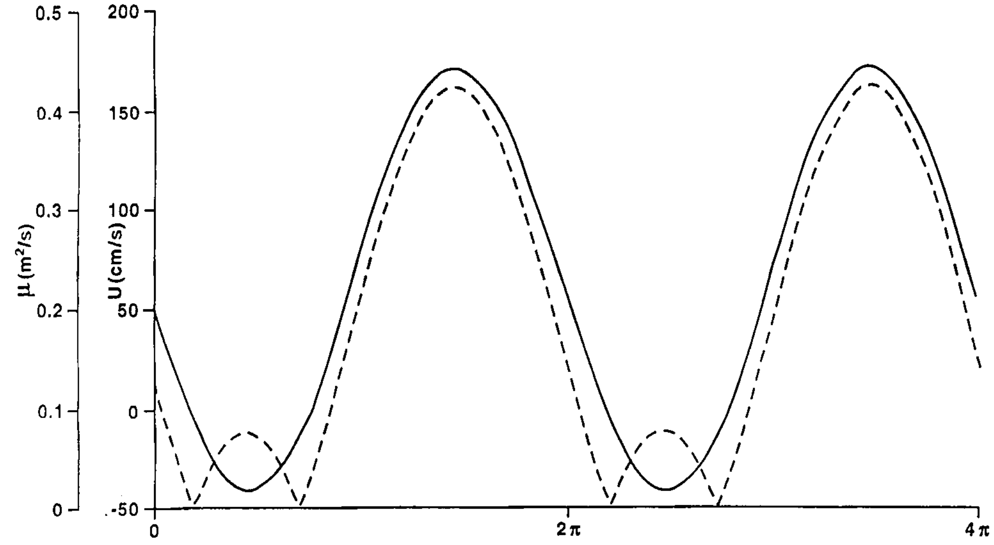

Figure 4(c). As Figure 4(b) but with $h = 100$ m

near mid-depth (Table II, Figure 4(a)). The generation of the higher harmonics is principally restricted to the D_6-harmonic (Table II).

The differences between the surface currents computed with the uniform and transformed grids in the case of $h = 100$ m but not $h = 10$ m can be partly explained by the difference in water depth, in that for a given eddy viscosity the shear is larger in deep than in shallow water (see Figure 3). However, to understand the slower rate of convergence in deep water, it is necessary to examine the time series of total current and surface viscosity (Figures 4(b) and 4(c)) over two tidal cycles. In shallow water (Figure 4(b)) the viscosity shows a maximum and a minimum value over a tidal cycle, with equal maxima and minima between tidal cycles, showing that a steady state periodic solution has been obtained corresponding to the maximum and minimum currents over a tidal cycle (Figure 4(b)). In the absence of wind the time series of the u-component of current for the rectilinear tide considered here would show equal positive and negative values over a tidal cycle. The wind forcing used here increases the u-component of current and in the case of $h = 10$ m the magnitude of the wind-induced current exceeds the amplitude of the tidal current, giving rise to the time series shown in Figure 4(b) in which the u-component of current remains positive. The eddy viscosity is a maximum at times of maximum flow and has a small but finite value at times of minimum flow.

In deeper water, $h = 100$ m, the magnitude of the wind-induced current is less than the tidal amplitude and the u-component of current is negative for part of the tidal cycle, with times of zero current (Figure 4(c)). Consequently, the corresponding eddy viscosity time series is more complex, with times of zero eddy viscosity when the surface shear must be infinite and hence cannot be resolved in the model. However, the differences between the various numerical approaches are restricted to the very-near-surface currents, with currents 1 m below the sea surface being in excellent agreement (Table II).

Rectilinear tidal flow with a no-slip condition (viscosity profile B). In the previous series of calculations a slip condition was used at the sea bed, with the eddy viscosity constant from sea surface to sea bed (Figure 2, profile A) and proportional to $h|\bar{u}|$. By using a slip condition, it was not necessary to resolve the near-bed logarithmic layer which occurs with a no-slip condition. In this series of calculations we use viscosity profile B (Figure 2) with a no-slip condition at the sea bed and hence include the bed logarithmic layer. The importance of resolving this layer using a logarithmic-type grid in the near-bed region for tidal flow problems was shown by Davies.[16] Since we are concerned here with both tidal and wind-driven flows, it is necessary to resolve both the surface and bed boundary layers.

Surface, near-surface, mid-depth and near-bed values of the residual current (D_0) and the amplitude and phase of the components D_2, D_4 and D_6 of the tide computed with both an $h|\bar{u}|$- and a $\bar{u}^2$-dependent viscosity and profile B in a water depth $h = 10\,m$ are given in Table III using both a uniform grid ($N = 100$) and an irregular grid together with the functional approach. The corresponding results in a water depth $h = 100$ m are given in Table IV. Consider initially the $h|\bar{u}|$-dependent viscosity. It is evident from Table III that with a uniform grid the magnitude of the near-bed current is less than that obtained with the irregular grid which can accurately resolve the high-shear layer (Figure 5(a)) which occurs in the near-bed region.[16] Currents computed with the irregular grid were found to be in excellent agreement with those determined using the functional approach (Table III). It is also clear from Table III and Figure 5(a) that as in the previous series of calculations (those involving a slip condition at the bed), the wind-driven residual (D_0) decreases uniformly with distance below the surface, with a rapid reduction close to the bed. The direct tidally forced component D_2 shows a mid-water maximum with a reduction in the surface layer and a rapid reduction close to the bed. The higher tidal harmonics D_4 and D_6 produced by the non-linear interaction of a time-varying eddy viscosity and the shear term $\partial u/\partial z$ are largest in the surface and bed boundary layers where $\partial u/\partial z$ is greatest.

Calculations using the $\bar{u}^2$-dependent viscosity in a water depth $h = 10$ m show significant differences in the magnitude of the surface current computed using a uniform grid, a double-

Table III. As Table II but using a no-slip condition at the sea bed with $h = 10$ m

		Uniform finite difference				Transformed finite difference				Functional method			
σ		D_0	D_2	D_4	D_6	D_0	D_2	D_4	D_6	D_0	D_2	D_4	D_6
						(a) $\mu \propto h\lvert\bar{u}\rvert$							
1·0	H	99	23	10	8	102	33	6	6	101	33	6	6
	g	—	189	85	139	—	202	80	144	—	201	82	146
0·95	H	94	27	7	6	98	37	4	5	98	36	5	5
	g	—	194	86	142	—	204	76	145	—	203	80	147
0·5	H	57	51	9	3	67	56	9	2	68	56	8	2
	g	—	208	276	339	—	211	287	354	—	211	287	354
0·05	H	27	38	9	4	40	46	9	3	40	47	10	3
	g	—	210	277	342	—	213	286	353	—	213	286	254
						(b) $\mu \propto \bar{u}^2$							
1·0	H	200	266	222	148	154	168	125	54	123	115	86	39
	g	—	48	93	143	—	49	93	140	—	54	101	158
0·95	H	95	72	63	44	98	72	59	31	99	74	59	30
	g	—	50	90	136	—	62	110	172	—	59	107	169
0·5	H	19	46	24	14	21	49	24	12	22	48	23	11
	g	—	210	264	322	—	215	278	348	—	214	277	348
0·05	H	1	43	24	13	2	52	27	14	3	52	26	13
	g	—	215	270	331	—	220	286	3	—	220	286	4

Table IV. As Table II but using a no-slip condition at the sea bed with $h = 100$ m

		Uniform finite difference				Transformed finite difference				Functional method			
σ		D_0	D_2	D_4	D_6	D_0	D_2	D_4	D_6	D_0	D_2	D_4	D_6
						(a) $\mu \propto h\lvert\bar{u}\rvert$							
1·0	H	67	94	109	10	76	91	9	11	75	92	7	8
	g	—	261	21	87	—	261	27	94	—	261	32	103
0·95	H	61	98	7	5	70	95	6	5	72	95	5	5
	g	—	261	43	104	—	261	47	116	—	261	45	114
0·5	H	34	103	2	2	42	104	2	2	44	104	2	2
	g	—	259	92	314	—	261	93	316	—	261	91	318
0·05	H	14	72	4	2	22	81	3	2	24	82	3	1
	g	—	249	291	265	—	254	305	305	—	255	308	311
						(b) $\mu \propto \bar{u}^2$							
1·0	H	178	103	172	180	120	54	42	56	102	71	19	23
	g	—	351	27	64	—	248	7	92	—	250	16	112
0·95	H	81	85	13	9	87	83	10	9	89	81	11	10
	g	—	256	34	136	—	253	32	148	—	252	28	137
0·5	H	32	105	4	3	39	106	4	3	40	106	4	3
	g	—	262	106	337	—	263	105	337	—	264	100	346
0·05	H	6	81	6	2	14	89	4	2	15	90	3	2
	g	—	252	301	280	—	258	314	321	—	258	318	334

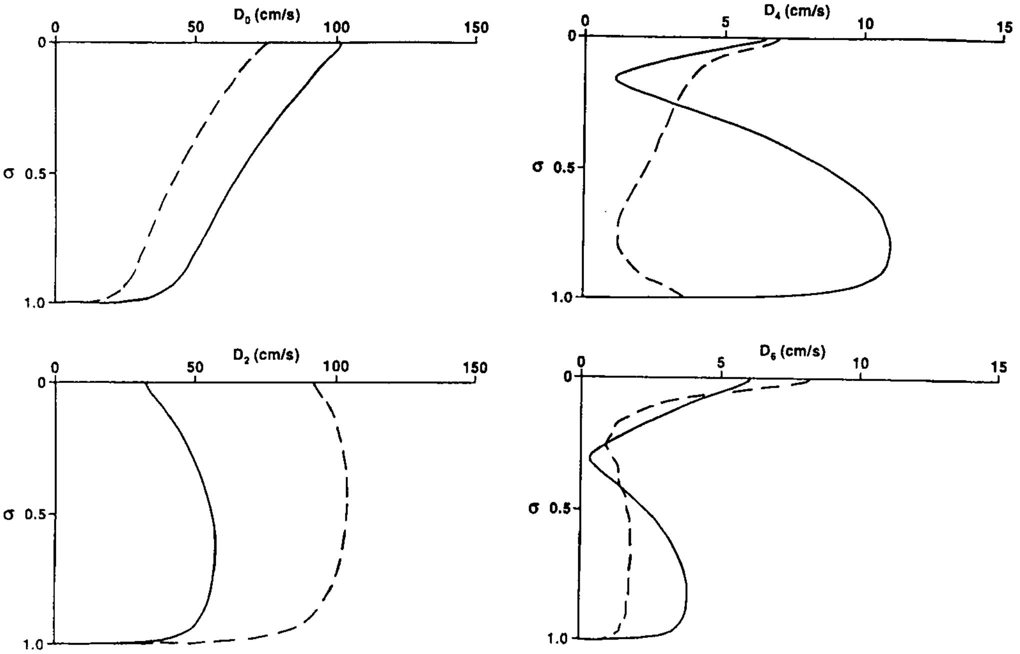

Figure 5(a). As Figure 4(a) in water depths $h = 10$ m (——) and $h = 100$ m (- - -) with $\mu \propto h|\bar{u}|$ but using a no-slip condition

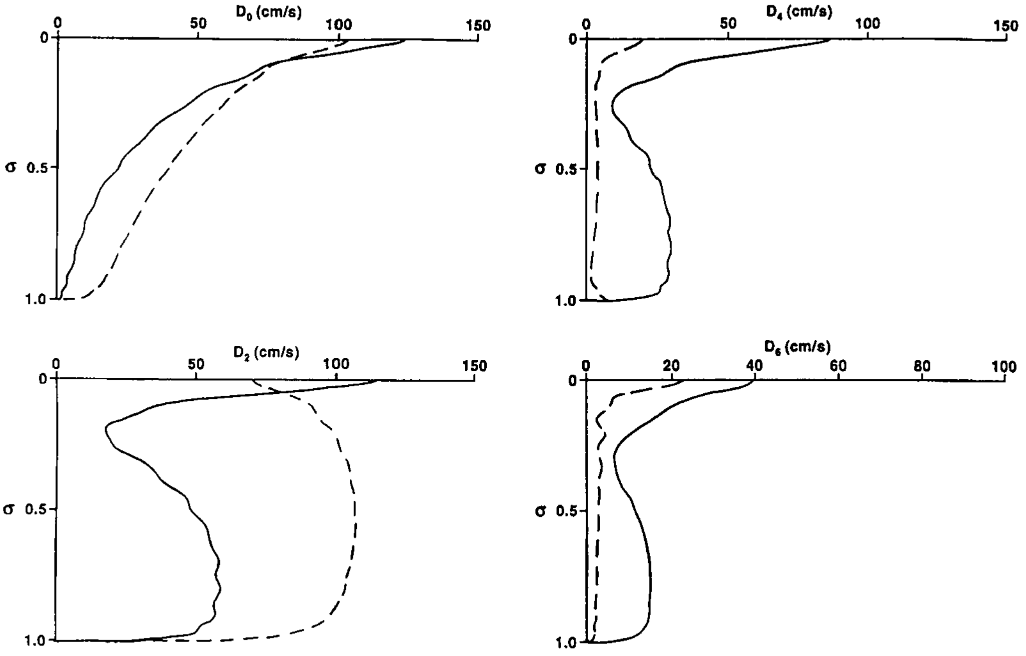

Figure 5(b). As Figure 5(a) but with $\mu \propto \bar{u}^2$

logarithmic grid or the functional approach (Table III), although these differences in the case of the double-logarithmic grid and functional approach are confined to the near-surface layer (Table III). Profiles (Figure 5(b)) and values (Table III) show that as with the $h|\bar{u}|$-dependent viscosity, D_0 decreases uniformly from sea surface to sea bed. However, D_2 does not exhibit a mid-water maximum but rather a minimum below the sea surface, with an increase rather than a decrease close to the sea surface, the reason for which is not apparent. The higher harmonics D_4 and D_6 are much larger in the case of the $\bar{u}^2$-dependent viscosity than in the case of the $h|\bar{u}|$-varying viscosity, again showing maximum values in the near-surface and near-bed shear layers (Table III, Figure 5(b)). To understand these differences in magnitude, it is instructive to examine time series of mid-depth currents and near-surface viscosities (Figure 6) and also to perform a Fourier analysis of the surface eddy viscosity time series over the same tidal cycle used in the current analysis. The time series of current (Figure 6(a)) in a water depth $h = 10$ m is very similar to that computed previously with the slip condition and shows a u-velocity varying over the tidal cycle but always remaining positive. Consequently, the corresponding time series of eddy viscosity (Figure 6(a)) is very similar to that found with a slip condition.

In the case of the $\bar{u}^2$-dependent viscosity the current varies significantly over the tidal cycle (Figure 6(b)) and the depth-mean current was zero or small for a significant part of the cycle, giving rise to the time series of viscosity shown in Figure 6(b). It is apparent from this figure that the viscosity is low for significant parts of the tidal cycle, giving rise to major convergence problems and what appear to be some slight instabilities in the current time series (Figure 6(b)). Also, the rapid changes in the time series of eddy viscosity shown in Figure 6(b) will give rise to higher harmonics than those produced with the $h|\bar{u}|$-dependent viscosity.

A Fourier analysis of the two viscosity time series showed that the amplitude of the eddy viscosity at the frequencies D_0, D_2, D_4 and D_6 (Table V) is about twice as large and at the frequency D_6 about five times as large with the $\bar{u}^2$-dependent viscosity as with the $h|\bar{u}|$-dependent viscosity, which partly explains the increased magnitude of the components D_6 and D_4 of the tide in the calculation with $\mu \propto \bar{u}^2$.

Calculations in deeper water, $h = 100$ m (Table IV, Figure 5(a) and 5(b)), with both an $h|\bar{u}|$- and a $\bar{u}^2$-dependent viscosity show an intensification in the amplitude of the component D_2 of the tide at mid-depth, although in this case the eddy viscosity is much larger (Table V) and this reduces the shear in the vertical.

Time series of current computed with both an $h|\bar{u}|$- and a $\bar{u}^2$-dependent viscosity (Figures 6(c) and 6(d)) in a water depth $h = 100$ m show an oscillatory tidal flow with a superimposed wind-induced current. The time series show current magnitudes in both cases varying from the order of 150 to -50 cm s^{-1}, giving rise to a time-varying eddy viscosity changing from zero to a maximum of the order of 0·4 m^2 s^{-1} (Figures 6(c) and 6(d))—values of viscosity an order of magnitude larger than those found with $h = 10$ m.

Time series of eddy viscosity (Figure 6) computed with both an $h|\bar{u}|$- and a $\bar{u}^2$-dependent viscosity in water depths $h = 10$ and 100 m clearly show that in shallow water the viscosity is much smaller and hence the surface shear much larger than in deep water. Also, the time variation with a $\bar{u}^2$-dependent viscosity is larger than with an $h|\bar{u}|$-dependent viscosity, thus explaining the differences in magnitude in the components D_4 and D_6 of the tide found in these calculations. Obviously it is not just the value of the amplitude of the viscosity at the various frequencies but the time variation of the total which produces time variations in the depth to which the wind's energy can diffuse.

Circular tidal flow with a no-slip condition (viscosity profile B). In the earlier calculations rotation was omitted, $\gamma = 0{\cdot}0$, and tidal forcing was only in the u-direction, with wind forcing

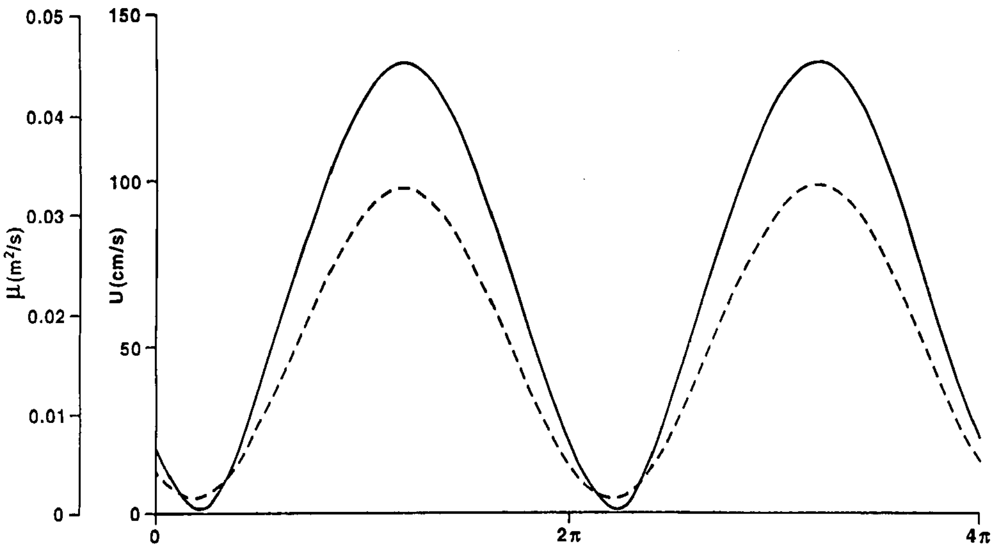

Figure 6(a)(b). Time series of current (——) and eddy viscosity (– – –) over two tidal cycles computed using a no-slip condition with $h = 10$ m, $\mu \propto h|\bar{u}|$, (b) $h = 10$ m, $\mu \propto \bar{u}^2$

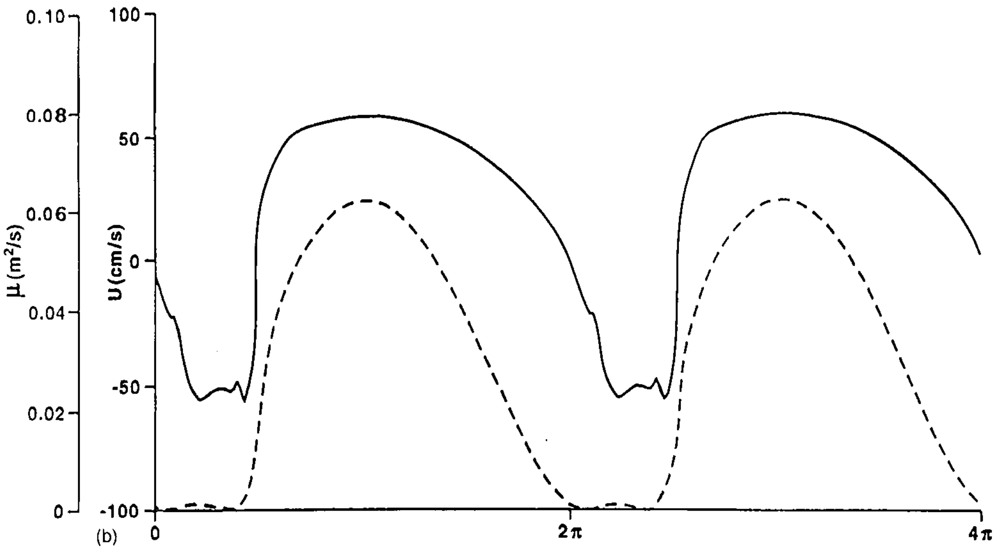

also in this direction. In this series of calculations rotation is also omitted but we consider an additional tidal forcing in the v-direction phase-shifted by 90° from the u-tidal forcing, giving a circular tidal ellipse, i.e. the magnitude of the tidal current, which is equal to $(u^2 + v^2)^{1/2}$, is constant. Consequently, in the absence of wind-driven currents a flow-related eddy viscosity of the form used previously would not show any time variability and hence in the single-point model considered here higher tidal harmonics would not be generated.[23] However, the addition

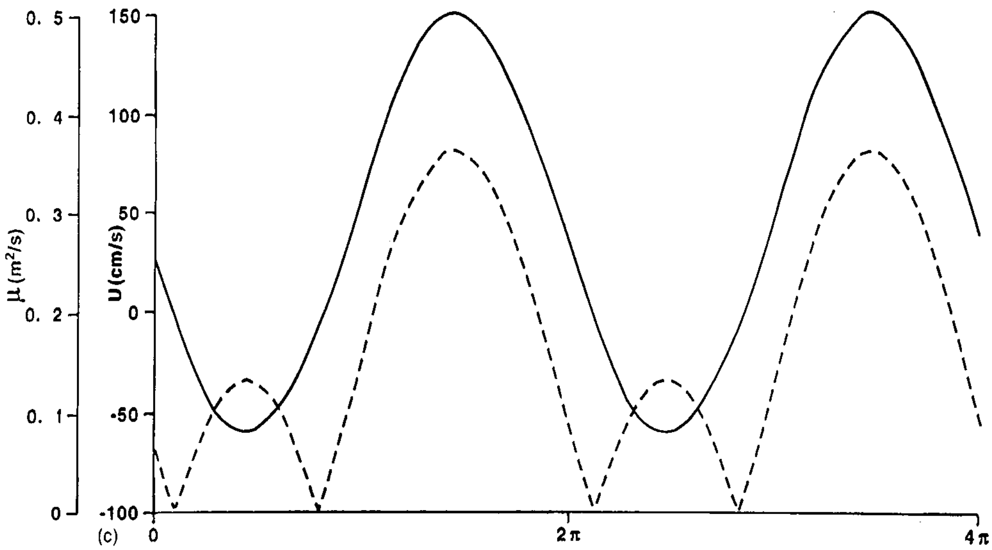

Figure 6(c)(d). As Figure 6(a) but with (c) $h = 100$ m, $\mu \propto h|\bar{u}|$ and (d) $h = 100$ m, $\mu \propto \bar{u}^2$

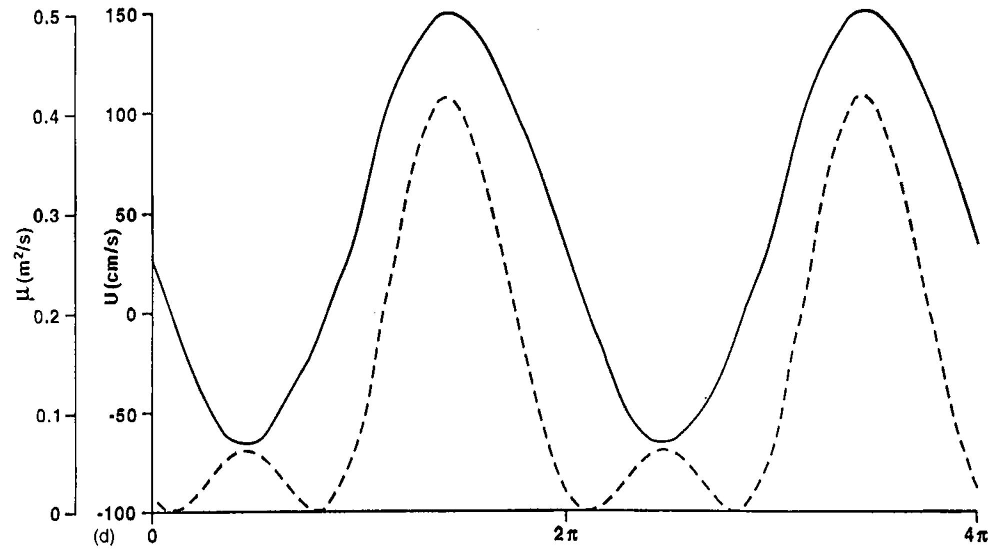

of a wind-forced current to the tidal current means that the eddy viscosity is no longer constant in time and higher harmonics and a residual flow can be generated in both the u- and v-directions (Tables VI and VII, Figures 7(a) and 7(b)). In an initial series of calculations a water depth $h = 10$ m was used. Calculations (Table VI) show that currents computed with an irregular log–linear grid using a $\bar{u}^2$-dependent viscosity are not significantly different from those computed with the functional model, with some minor differences in the two approaches occurring using

Table V. Amplitude H (cm^2 s^{-2}) and phase g (deg) at frequencies D_0, D_2, D_4 and D_6 determined by Fourier analysis of the eddy viscosity time series

$h = 10$ m		D_0	D_2	D_4	D_6
	(a) Rectilinear tidal flow				
$\mu \propto h\|\bar{u}\|$	H	163	121	17	4
	g	—	209	284	4
$\mu \propto \bar{u}^2$	H	281	291	37	22
	g	—	197	285	32
$h = 100$ m					
$\mu \propto h\|\bar{u}\|$	H	1820	1220	900	343
	g	—	260	161	250
$\mu \propto \bar{u}^2$	H	1338	1546	1030	84
	g	—	260	161	329
	(b) Circular tidal flow (no slip)				
$h = 10$ m					
$\mu \propto h\|\bar{u}\|$	H	218	120	40	19
	g	—	218	281	344
$\mu \propto \bar{u}^2$	H	456	283	91	43
	g	—	200	246	302
$h = 100$ m					
$\mu \propto h\|\bar{u}\|$	H	2802	1035	106	20
	g	—	261	357	81
$\mu \propto \bar{u}^2$	H	2385	1508	73	3
	g	—	261	65	258

a $h|\bar{u}|$-dependent viscosity. In the case of the $\bar{u}^2$-dependent viscosity the amplitude of the viscosity at all frequencies is much larger (Table V), leading to a faster rate of convergence of the grid box model owing to the reduced shear in the vertical (Table VI). It is evident from Table VI and Figure 7(a) that the D_0-component of current in the wind direction exhibits a uniform decrease through the vertical above a high-shear bottom boundary layer, with that computed using the $\bar{u}^2$-dependent viscosity being significantly lower than that found with the $h|\bar{u}|$-dependent viscosity because of the larger viscosity arising with the $\bar{u}^2$-formulation.

As in the previous series of calculations using a rectilinear tidal flow, the D_2-component of current in the wind direction (the u-component) shows a mid-water maximum (Figure 7(a), Table VI), with the D_2-component orthogonal to the wind direction (the v-component) showing the 'classical' tidal current profile of nearly constant velocity (Table VI) above a high-shear bottom boundary layer.

The non-linearity in the equations due to the time-varying viscosity produces currents at the tidal frequencies D_2 and D_4 in both the u- and v-components (Figure 7(a), Table VI) in a similar manner to that occurring with the rectilinear tidal flow. Also, it is interesting to note that a small tidal residual (the D_0-frequency) is produced in the v-direction owing to the time-varying eddy viscosity. A similar residual will occur in the u-direction, but this is combined with the wind-driven residual and cannot be separated by Fourier analysis.

Table VI. Computed u- and v-components of amplitude H (cm s^{-1}) and phase g (deg) at residual D_0 and tidal periods D_2, D_4 and D_6 using wind forcing and a circular tidal current ellipse in a water depth h = 10 m with a no-slip bottom boundary condition

		Transformed finite difference grid				Functional method			
σ		D_0	D_2	D_4	D_6	D_0	D_2	D_4	D_6
				(a) $\mu \propto h\lvert\bar{u}\rvert$					
				u-component					
1·0	H	90	42	12	11	88	42	11	11
	g	—	206	110	169	—	205	112	170
0·5	H	59	59	6	3	58	59	6	3
	g	—	215	286	349	—	214	287	351
0·05	H	36	47	7	4	36	47	7	4
	g	—	216	290	357	—	216	291	359
				v-component					
1·0	H	−3	74	8	2	−3	73	8	2
	g	—	134	233	313	—	134	230	315
0·5	H	−2	68	7	2	−3	68	7	2
	g	—	133	228	305	—	133	226	306
0·05	H	−1	49	5	1	−2	49	5	1
	g	—	131	218	280	—	131	216	282
				(b) $\mu \propto \bar{u}^2$					
				u-component					
1·0	H	42	23	5	7	41	24	5	6
	g	—	196	72	118	—	196	69	114
0·5	H	25	37	7	3	25	36	7	3
	g	—	204	262	312	—	203	262	313
0·05	H	14	29	7	4	14	29	7	4
	g	—	205	262	312	—	205	262	312
				v-component					
1·0	H	−2	45	9	3	−3	45	8	4
	g	—	118	181	245	—	117	178	243
0·5	H	−2	42	8	3	−2	42	8	3
	g	—	117	179	240	—	117	176	239
0·05	H	−1	30	6	2	−2	30	5	2
	g	—	116	174	229	—	115	171	229

Currents in deeper water (h = 100 m) computed using both the $h|\bar{u}|$- and the $\bar{u}^2$-dependent viscosity with the irregular double-log–linear grid and the functional approach are in much closer agreement (Table VII) than in the shallower water case. The reason for this is that the eddy viscosity is an order of magnitude higher (Table V) and hence the shear is reduced (compare Figure 7(b) with Figure 7(a)), so both approaches converge much more rapidly. Although the amplitudes of the D_2- and (in the case of $\mu \propto h|\bar{u}|$) D_4-components of the eddy viscosity are much larger and therefore the time variability of the viscosity is higher than in the shallow water case, it is evident from Table VII that the D_4- and D_6-components are smaller. The reason for this is that the higher eddy viscosity in this calculation reduces the shear in the

Table VII. As Table VI but with $h = 100$ m

		Transformed finite difference grid				Functional method			
σ		D_0	D_2	D_4	D_6	D_0	D_2	D_4	D_6
				(a) $\mu \propto h\lvert\bar{u}\rvert$					
				u-component					
1·0	H	55	103	1	0	56	103	1	0
	g	—	262	132	—	—	262	134	—
0·5	H	38	102	1	0	39	102	1	0
	g	—	260	56	—	—	260	57	—
0·05	H	23	75	1	0	24	76	1	0
	g	—	256	12	—	—	256	15	—
				v-component					
1·0	H	0	107	2	0	−1	107	2	0
	g	—	174	7	—	—	173	6	—
0·5	H	0	101	1	0	0	101	1	0
	g	—	171	333	—	—	171	332	—
0·05	H	0	74	1	0	1	75	1	0
	g	—	165	262	—	—	166	263	—
				(b) $\mu \propto \bar{u}^2$					
				u-component					
1·0	H	57	97	3	0	57	97	2	0
	g	—	261	163	—	—	261	167	—
0·5	H	34	103	3	0	35	103	3	0
	g	—	261	58	—	—	261	60	—
0·05	H	18	78	2	0	19	79	2	0
	g	—	257	19	—	—	257	23	—
				v-component					
1·0	H	−3	106	2	0	−3	106	2	0
	g	—	175	19	—	—	175	20	—
0·5	H	−1	102	2	0	−1	102	2	0
	g	—	172	337	—	—	172	337	—
0·05	H	2	76	2	0	2	77	3	0
	g	—	165	262	—	—	167	263	—

vertical and hence the ability of the non-linear term $\mu \partial u/\partial z$ to transfer energy to the higher harmonics.

Although rotational effects have been neglected in order to clearly demonstrate how wind forcing in the u-direction can lead to a residual flow in the v-direction, their inclusion is essential in any physically realistic simulation.[24] Also, a quadratic bottom friction (equation (7)) rather than a linear friction is necessary in any 'real-world' model and the non-linearity that this introduces will itself produce higher tidal harmonics in addition to those due to the time-varying viscosity.

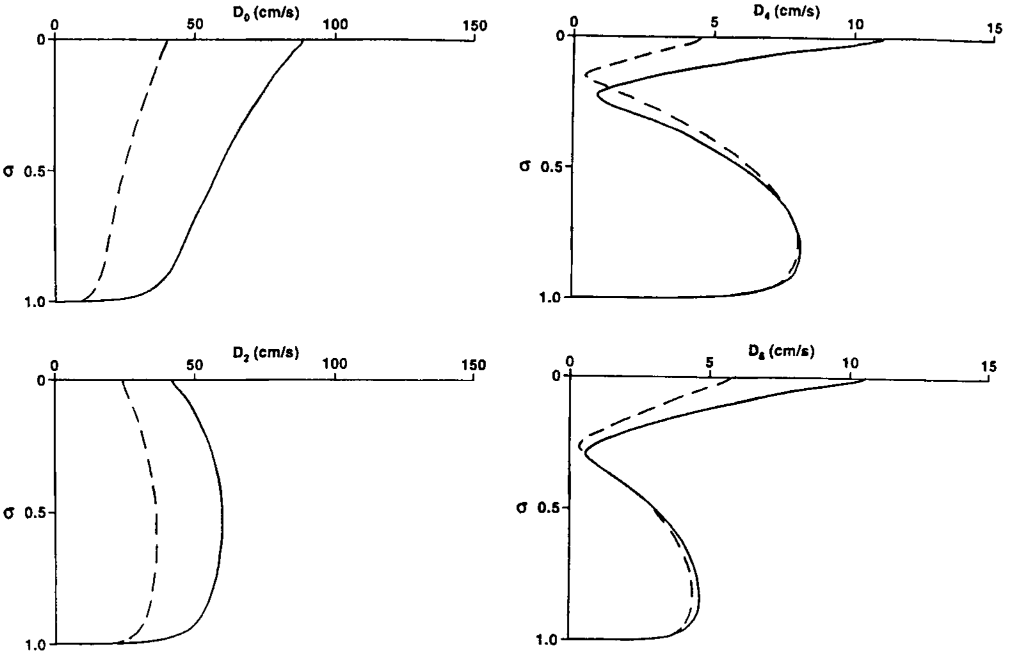

Figure 7(a). Profiles of u-component of residual current (D_0) and harmonics D_2, D_4 and D_6 computed using a circular tidal current ellipse with a no-slip condition in a water depth $h = 10$ m with $\mu \propto h|\bar{u}|$ (——) and $\mu \propto \bar{u}^2$ (- - -)

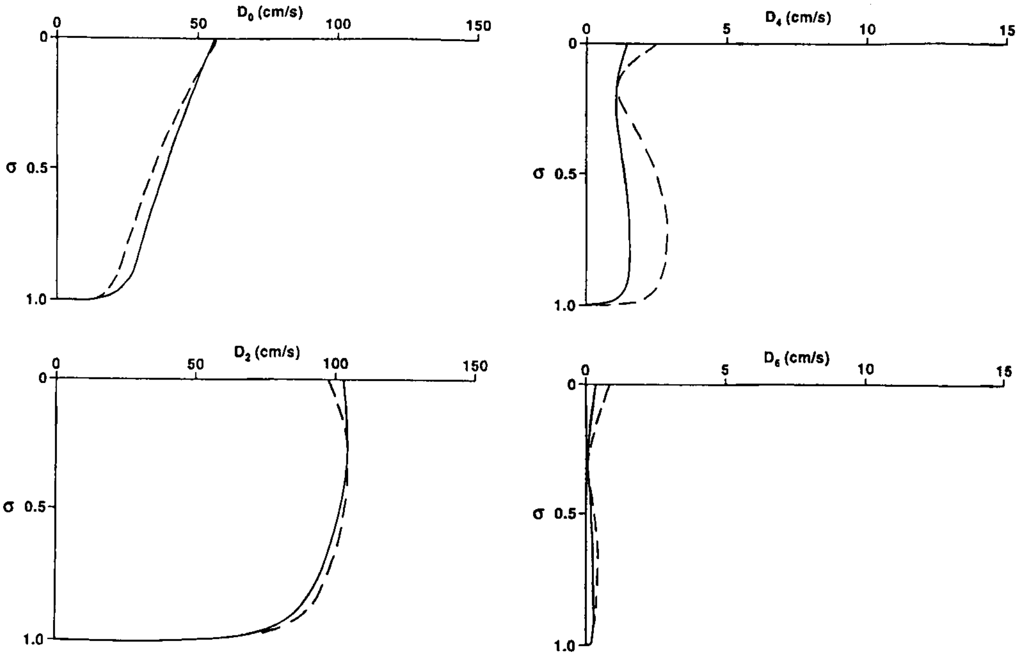

Figure 7(b). As Figure 7(a) but with $h = 100$ m

4. CONCLUDING REMARKS

An idealized single-point model in the vertical has been used to examine the non-linear interaction between wind-induced and tidally forced currents due to time variations in the eddy viscosity. Calculations have been made using a uniform finite difference grid in the vertical with an increasing number of grid boxes and using an irregularly spaced grid with a log–linear compression in both the surface and bed regions. Complementary calculations using a functional approach have been performed to check the accuracy of the solution, in particular that the same non-linear interaction is found in both solutions and hence it is a physically real process rather than a property of the numerical method.

Calculations using the uniform grid show that for low eddy viscosity values a large number of grid points are required to ensure sufficient resolution in the high-shear surface and bed boundary layers, particularly with a no-slip bottom boundary condition where a logarithmic layer can occur. For tidal flows subject to a no-slip bed condition, Davies[16] showed that a logarithmic or log–linear compression in the near-bed region was essential to ensure computational accuracy without using an excessive number of grid points in the vertical. The calculations performed here show that with log–linear-compressed grids in the surface and bed boundary layers, accurate solutions in good agreement with those obtained using a functional approach are possible.

For the linear model considered here, if the eddy viscosity is constant, then the wind-induced and tidally induced current profiles are independent and no coupling can occur. However, by using a flow-dependent, more physically realistic eddy viscosity which varies with time, coupling can occur between the wind-induced current and that of tidal origin. The intensity of this coupling depends upon the time variability of the eddy viscosity and the magnitude of current shear in the vertical. Since the shear is largest in the surface and bed boundary layers, theory and calculations show that maximum coupling of the flows will occur in these regions, leading to a decrease at the sea surface in the amplitude of the D_2-tide and the production of D_4- and D_6-harmonics in these regions.

The significant change in the vertical profile of the D_2-tide with a reduction in the surface boundary layer is consistent with results of simulations of tidal and wind-induced currents in the Eastern Irish Sea.[24] The results from the simple model described here confirm that this is a physically realistic effect and go some way to explaining the mechanisms producing it. More physically realistic calculations using an Eastern Irish Sea model are presently in progress and will be reported subsequently.[24]

ACKNOWLEDGEMENTS

One author (J. L.) would like to express his thanks to the Director of POL for computing and other facilities during his stay and to MAFF for a year's leave of absence.

The care taken by Mr. R. A. Smith in preparing diagrams and Mrs. J. Hardcastle in typing the text is appreciated.

REFERENCES

1. A. M. Davies, 'A three-dimensional model of the northwest European continental shelf with application to the M_4 tide', *J. Phys. Oceanogr.*, **16**, 797–813 (1986).
2. B. Galerperin and G. L. Mellor, 'A time-dependent, three dimensional model of the Delaware Bay and river system. Part 2. Three-dimensional flow fields and residual circulation', *Estuar. Coastal Shelf Seas*, **31**, 231–255 (1990).
3. R. B. Gordon and M. L. Spaulding, 'Numerical simulations of the tidal- and wind-driven circulation in Narragansett Bay', *Estuar., Coastal Shelf Sci.*, **24**, 611–636 (1987).

4. J. N. Aldridge and A. M. Davies, 'A high resolution three dimensional hydodynamic tidal model of the Eastern Irish Sea', *J. Phys. Oceanogr.*, **23**, 207–224 (1992).
5. A. M. Davies and J. E. Jones, 'Application of a three-dimensional turbulence energy model to the determination of tidal currents on the northwest European shelf', *J. Geophys. Res.*, **95**, 18,143–18,162 (1990).
6. A. M. Davies and J. E. Jones, 'A three dimensional model of the M_2, S_2, N_2, K_1 and O_1 tides in the Celtic and Irish Seas', *Prog. Oceanogr.*, **29**, 197–234 (1992).
7. A. M. Davies, 'Three dimensional modelling of surges', D. H. Peregrine (ed.), *Floods due to High Winds and Tides*, Academic, New York, 1981, pp. 45–74.
8. A. M. Davies, 'Meteorologically-induced circulation on the north west European continental shelf: from a three-dimensional numerical model', *Oceanol. Acta*, **5**, 269–280 (1982).
9. A. M. Davies and J. E. Jones, 'A three-dimensional wind driven circulation model of the Celtic and Irish Seas', *Continental Shelf Res.*, **12**, 159–188 (1992).
10. K. F. Bowden, 'Physical problems of the benthic boundary layer', *Geophys. Surv.*, **3**, 255–296 (1978).
11. K. F. Bowden, L. A. Fairbairn and P. Hughes, 'The distribution of shearing stresses in a tidal current', *Geophys. J. R. Astronom. Soc.*, **2**, 288–305 (1959).
12. K. F. Bowden and S. R. Ferguson, 'Variations with height of the turbulence in a tidally-induced bottom boundary layer', in J. C. J. Nihoul (ed.), *Marine Turbulence, Proc. 11th Int. Liege Colloq. on Ocean Hydrodynamics*, Elsevier, Amsterdam, 1979, pp. 259–286.
13. A. M. Davies, 'Formulation of a linear three-dimensional hydrodynamic sea model using a Galerkin–eigenfunction method', *Int. j. numer. methods fluids*, **3**, 33–60 (1983).
14. A. M. Davies, 'Spectral models in continental shelf sea oceanography', in N. S. Heaps (ed.), *Coastal and Estuarine Sciences*, No. 4, *Three-dimensional Coastal Ocean Models*, American Geophysical Union, Washington, DC, 1987, pp. 71–106.
15. A. M. Davies, 'Solution of the 3D linear hydrodynamic equations using an enhanced eigenfunction approach', *Int. j. numer. methods fluids*, **13**, 235–250 (1991).
16. A. M. Davies, 'On the accuracy of finite difference and modal methods for computing tidal and wind wave current profiles', *Int. j. numer. methods fluids*, **12**, 101–124 (1991).
17. A. M. Davies, 'Modelling currents in highly sheared surface and bed boundary layers', *Continental Shelf Res.*, **12**, 189–211 (1992).
18. R. W. Lardner, 'Numerical solution of the linearized three-dimensional tidal equations using eddy viscosity eigenfunctions', *J. Geophys. Res.*, **95**, (C12), 22,269–22,274 (1990).
19. T. J. Zitman, 'Quasi three-dimensional current modelling based on a modified version of Davies' shapefunction approach', *Continental Shelf Res.*, **12**, 143–158 (1992).
20. A. M. Davies, 'A bottom boundary layer resolving three dimensional tidal model: a sensitivity study of eddy viscosity formulation', *J. Phys. Oceanogr.*, **23**, 1437–1453.
21. A. M. Davies, 'A three dimensional modal model of wind induced flow in a sea region', *Prog. Oceanogr.*, **15**, 71–128 (1985).
22. A. M. Davies and J. Aldridge, 'A numerical model study of parameters influencing tidal currents in the Irish Sea', *J. Geophys. Res.*, **98**, 7049–7067 (1993).
23. A. M. Davies, 'On the importance of time varying eddy viscosity in generating higher tidal harmonics', *J. Geophys. Res.*, **95**, 20,287–20,312 (1990).
24. A. M. Davies and J. Lawrence, 'Examining the influence of wind and wind–wave turbulence on tidal currents, using a three dimensional hydrodynamic model including wave–current interaction', *J. Phys. Oceanogr.*, in press.